

Investigation of links between dynamical scenarios and particularly high impact of Aeolus on NWP forecasts

Anne Martin¹, Martin Weissmann², and Alexander Cress³

¹Ludwig-Maximilians-Universität, Meteorologisches Institut, München, Germany

²Universität Wien, Institut für Meteorologie und Geophysik, Wien, Austria

³Deutscher Wetterdienst (DWD), Offenbach am Main, Germany

Correspondence: Anne Martin (anne.martin@physik.uni-muenchen.de)

Abstract. Global wind profiles from the Aeolus satellite mission provide an important source of wind information for Numerical Weather Prediction (NWP). Data assimilation experiments show large mean changes in the analysis and a significant reduction of forecast errors. At Deutscher Wetterdienst (DWD), an Observing Systems Experiment (OSE) for three months, from July 2020 to October 2020, has been performed to evaluate the impact of the Aeolus horizontal line-of-sight (HLOS) wind observations in the operational data assimilation system of the ICOSahedral Nonhydrostatic (ICON) global model. To better understand the underlying dynamics leading to the overall beneficial impact, specific time periods and regions with particularly high impact of Aeolus are investigated. In this study, we illustrate three examples of atmospheric phenomena that constitute dynamical scenarios for significant forecast error reduction through the assimilation of Aeolus: The phase shift of large-scale tropical circulation systems, namely the quasi-biennial oscillation (QBO) and the El Niño–Southern Oscillation (ENSO), and the interaction of tropical cyclones undergoing extratropical transition (ET) with the midlatitude waveguide.

1 Introduction

The Aeolus satellite mission from the European Space Agency (ESA) provides a novel data set of actively-sensed wind profiles with quasi-global coverage intended to compensate for deficiencies of the current Global Observing System (GOS). Besides other scientific and technological developments, advances in the operational assimilation of satellite observations have been one of the major contributing factors to the increase in Numerical Weather Prediction (NWP) skill over the last decade (Bauer et al., 2015). However, the information available from satellite instruments is not always directly related to the fundamental variables of the model and the global observing system is heavily biased towards mass observations (Baker et al., 2014). This can be a strong limitation in regions and for spatial scales where the geostrophically mass-wind coupling is weak and the atmospheric dynamics are mainly determined by the wind field. Therefore, direct wind profile information from the Aeolus satellite is expected to be particularly efficient in NWP for the understanding of tropical dynamics on all length scales and the prediction of smaller-scale phenomena at higher latitudes (ESA, 2008). Furthermore, the ESA Mission Advisory team highlighted potential benefits from the Aeolus wind observations for improvements in the characterization of severe and intense storm developments and scale interaction processes associated with atmospheric wave activity (ESA, 1999, 2008, 2016).

The Aeolus satellite carries a Doppler Wind Lidar (DWL) instrument that can receive the backscatter signal from molecules (Rayleigh channel) and particles (Mie channel) up to a maximum measurement altitude of about 17 - 25 km. The wind product suitable for the use in NWP is the horizontal projection of the line-of-sight (HLOS) wind component. In parallel with the technical development of the Aeolus mission, several scientific and campaign activities were carried out to evaluate the potential of the HLOS observations for NWP. Adding simulated ADM Aeolus-like lidar observations to the GOS has been found to reduce forecast errors for poorly predicted severe weather events (Marseille et al., 2008a, b), in the 500 hPa average medium-range wind forecast over the Northern Hemisphere (Stoffelen et al., 2006), for the analysis and forecasts over oceans (Tan et al., 2007) and for tropical wave dynamics (Žagar, 2004; Žagar et al., 2008). Furthermore, DWL instruments were used at research flights during measurement campaigns over the North-Atlantic (A-TReC) and the Asian Pacific Ocean (T-PARC). Their assimilation into global NWP models led to a significant impact on the analysis and forecasts over Europe and around the development of tropical cyclones, as well as their interaction with the midlatitude waveguide (Pu et al., 2010; Weissmann and Cardinali, 2007; Weissmann et al., 2012). Since the launch of the Aeolus satellite in August 2018, several observing system experiment (OSE) studies have been conducted to investigate the impact of the Rayleigh and Mie HLOS wind observations in various NWP models (Garrett et al., 2022; Laroche and St-James, 2022; Pourret et al., 2022; Rennie et al., 2021). Most of these studies concentrated on global forecast error statistics showing overall large improvements. Particularly large impact of assimilating Aeolus observations was found for the 2-3 day wind and temperature forecasts in the tropical upper troposphere and lower stratosphere and in the Southern Hemisphere. In the Northern Hemisphere, Aeolus HLOS winds were found to have a less pronounced but still a relatively large influence on average compared to other observing systems.

Martin et al. (2022) performed an OSE for three months, from July 2020 to October 2020, using the global ICOSahedral Nonhydrostatic model (ICON) of DWD. The study introduced the experimental setup, the data quality and consistency and provided an overview of the systematic changes in the analysis and impact on forecast error. The results overall confirms the promising statistical improvements demonstrated in the global impact studies of Garrett et al. (2022); Laroche and St-James (2022); Pourret et al. (2022) and Rennie et al. (2021).

Using the OSE from Martin et al. (2022), this study aims to further investigate specific dynamical changes and processes related to the positive impact of Aeolus observations and to document dynamical scenarios that lead to particularly high forecast error reduction. In the tropics, two weeks of large improvement in the East Pacific west of the Peruvian coast and about five weeks in the global equatorial band in the stratosphere particularly stand out. These regions and periods are associated with a change in phase of the large-scale tropical circulation systems, the El Niño-Southern Oscillation (ENSO) and the Quasi-Biennial Oscillation (QBO). In addition, we focus on the midlatitudes, where spatiotemporal surveys show large forecast error reduction following the extratropical transition (ET) of tropical cyclones and their interaction with the midlatitude waveguide.

The outline of this paper is as follows: Details about the Aeolus observations and the experimental design, including the quality control criteria and verification methods, are described in Section 2. Section 3 provides a global overview of the Aeolus impact in the ICON model and motivates the further investigation of selected regions and periods. Section 4 examines the relation of the impact of Aeolus to specific atmospheric features such as the variability in the stratospheric jet (QBO), the El Niño–Southern Oscillation (ENSO) state change in the equatorial Eastern Pacific and the extratropical transition (ET) of

tropical cyclones in association with synoptic-scale Rossby wave packets (RWPs). Finally, Section 5 summarizes the study's
60 main conclusions.

2 Data and methods

2.1 Aeolus HLOS observations

The Doppler Wind Lidar (DWL) onboard the Aeolus satellite consists of a dual channel receiver analyzing the Doppler shift from the narrowband Mie and the broadband Rayleigh backscatter separately. The signals are detected and binned into 24 range
65 bins that can be varied along orbit from a minimum vertical resolution of 250 m to 2000 m and thus be adjusted to the needs of science applications and NWP. Typically, the uppermost measurement altitude is about 17 - 25 km. Horizontally, a minimum along-track resolution of 2.9 km (temporal resolution of 0.4 s) is achieved by accumulating 20 laser pulses and referred to as one "measurement". The operational on-ground processing of the different Aeolus products is performed near-real-time (NRT) at the European Centre for Medium-Range Weather Forecast (ECMWF). The Aeolus level-2B (L2B) wind product contains
70 the HLOS wind observations used for NWP. To control the horizontal resolution and achieve a sufficient signal-to-noise ratio, the measurements are grouped according to a scene-classification procedure into a type "clear" or "cloudy" (Tan et al., 2008). Therefore, measurement-scale optical properties, e.g., scattering ratio or particle extinction coefficient, are used to determine how much particulate and molecular backscatter contributes to the signal of an accumulated measurement bin. Four wind observation types are available: Rayleigh-clear and -cloudy with a horizontal average length of about 90 km and Mie-clear and
75 -cloudy, representing a horizontal mean of 10 km. A key step within the L2B processing chain is the correction for temperature and pressure-dependent Doppler broadening in the molecular backscatter signal (Rayleigh–Brillouin correction). This uses a series of auxiliary files containing information about, e.g. geolocation, calibration, and error estimates for several variables, as well as a prior (AUX_MET) data of atmospheric temperature and pressure from a short-range forecast (Šavli et al., 2021). The L2B processor provides several additional output data, such as uncertainty estimates or quality flags for the wind observations,
80 which are useful for data assimilation systems. The Aeolus data processing of the OSE period includes a NRT bias correction method. During the first part of the mission, validation studies showed large systematic differences, which vary seasonally, spatially and with orbital phase - particularly pronounced for the Rayleigh wind observations (e.g. Martin et al., 2021a; Rennie et al., 2021). These detected bias dependencies were found to be related to long-wave and solar radiation fluctuations and the radiative response to which the spectrometers of the DWL are very sensitive. The operationally implemented bias correction
85 is based on a multiple linear regression method of ECMWF O-B statistics and the thermistors of the telescope M1-mirror, eliminating most part of the bias (Weiler et al., 2021).

2.2 Model and experimental design

This section provides a brief description of the model and the experimental set up. For further information please refer to Martin et al. (2022). In this study, the impact of the Aeolus L2B HLOS wind observations is assessed using an experiment

90 with the operational version of the ICON model at DWD that is based on the non-hydrostatic system of equations in the global domain (Zängl et al., 2015). In the current operational version, the atmosphere is resolved by an icosahedral grid of 13 km horizontal mesh size and 90 layers in the vertical. The core module of the global data assimilation system is a Hybrid Variational Ensemble Kalman Filter (VarEnKF) combining the flow-dependent background error covariance matrix from a Local Ensemble Transform Kalman Filter (LETKF) with the static covariance matrix from the 3-dimensional Variational Data
 95 Assimilation system (3D-Var) (Reinert et al., 2023). This combination allows the inclusion of the time-varying background error structures and thus a better weighting of observations and background. The LETKF is based on a 40-member ensemble with a horizontal resolution of 40 km. The assimilation is carried out with a 3 h cycling (00, 03, ..., 18, 21 UTC). A 3 h short-term forecast serves as background field that is adjusted using all observations within ± 1.5 h around the corresponding time step to generate the analysis field from which the next forecast is initialized.

100 The impact of an existing observation network in an NWP model can be estimated by conducting OSEs. In an OSE, two continuous assimilation cycles are performed: A control run which typically uses the operational model and observation data set, and an experimental run in which the observation type of interest is either added or removed. Comparisons of the resulting analyses and corresponding forecasts then serve as the basis for impact studies. As described in Martin et al. (2022), the control run (CTRL) was performed without Aeolus but with all other operationally used observation types assimilated. The
 105 observations assimilated operationally are mainly radiances that account for $\sim 64\%$ of the total observations. Winds from scatterometers, satellite imagery, and GNSS signals together constitute about 18%. Conventional observations from aircraft reports, radiosondes, surface stations, buoys, pilot and wind profiler represent $\sim 7\%$ of the total number of observations. The proportion of assimilated wind profiles from the spaceborne lidar of the Aeolus mission is about 2% ($\sim 20,500$ HLOS wind observations per assimilation cycle). In the experimental run (EXP_A), the Rayleigh and Mie HLOS wind observations have
 110 been assimilated in addition to all other observation types. Both assimilation experiments were conducted with a corresponding cycled LETKF ensemble run to provide individual background error covariance estimates for the experiments. For EXP_A, the model background winds u and v have been interpolated to the Aeolus observation geolocation point (latitude, longitude, and height) and transformed to the Aeolus HLOS wind equivalents using the azimuth angle ϕ , which is defined as the angle of the LOS pointing vector of the laser projected onto the horizontal plane measured clockwise from north:

$$115 \quad HLOS = -u \sin \phi - v \cos \phi. \quad (1)$$

ϕ is provided as part of the observation geolocation information by the L2B product, being typical $\sim 260^\circ$ for ascending and $\sim 100^\circ$ for descending orbits. Assuming the HLOS winds as point observations with neglected vertical velocity is a reasonable approach since the averaging length scale of the Rayleigh HLOS winds is approximately the same size as the effective model resolution of ICON (between 80 and 100 km in the horizontal and between a few hundred meters in the lower troposphere up
 120 to 2 km in the stratosphere). The Mie winds' averaging box is about a factor of 10 smaller, but no thinning is applied. The assigned observation error for EXP_A was derived based on the Desroziers method (Desroziers et al., 2005) and provided in a table-driven format (Martin et al., 2022). It is the smallest in the middle troposphere and increases towards the lower as well as stratospheric levels.

2.2.1 Quality control settings for the OSE

- 125 To optimize the use of the L2B wind observations in the ICON model, the following quality control was applied before the assimilation:
- only observations with valid overall confidence flags have been used;
 - only the observation types Rayleigh-clear and Mie-cloudy winds were used, as they are generally of better quality than the other two observation types;
- 130
- Rayleigh winds with range-bin thicknesses of 250 m were rejected because of excessive noise;
 - Rayleigh winds with a horizontal accumulation length < 60 km and Mie winds with horizontal accumulation length < 5 km were rejected due to a large number of outliers in observation departure statistics;
 - Rayleigh winds with an L2B processor estimated observation error $> 8 \text{ m s}^{-1}$ were excluded;
 - Mie winds with an L2B processor estimated observation error $> 6 \text{ m s}^{-1}$ were excluded.
- 135 These quality control criteria were found to be reasonable in a preceding validation study (Martin et al., 2021a). The OSE for this study covers the Northern Hemisphere summer, July 2020 - October 2020. Although the operationally implemented telescope primary mirror M1 bias correction is very effective, the DWD system still shows a small residual bias that depends on altitude for the Rayleigh wind observations. Therefore, a model-based bias correction scheme has been applied to the Rayleigh and Mie wind observations. The bias correction, is a function of latitude and conducted for specific height levels: surface - 850
- 140 hPa, 850 - 500 hPa, 500 - 200 hPa, 200 - 70 hPa, 70 - 5 hPa. The bias correction values are derived from the previous seven days and separately for ascending and descending orbits. More details can be found in Martin et al. (2022).

2.2.2 Verification data and method

- In general, forecast errors are defined as the differences between the forecast provided by a NWP model and the true atmospheric state. To assess the systematic impact of the Aeolus HLOS wind observations in the OSE, we compare the forecast
- 145 errors of the CTRL and EXP_A experiment. Therefore, ERA5 reanalyses are used as verification data set. The ERA5 output is produced using the 4D-Var data assimilation of the ECMWF IFS at a horizontal resolution of 31 km and with 137 vertical model levels up to the height of 80 km (from 1000 hPa to 1 hPa, with 40 levels below 5 km) (Hersbach et al., 2020). As ERA5 reanalyses are based on a different model with different resolution compared to the OSE, they provide a relatively independent data source. The higher vertical resolution of ERA5 allows finer details of atmospheric phenomena to be resolved, such as a
- 150 more realistic representation of atmospheric waves and their interaction with the mean flow, which is especially crucial for the study of QBO in Sec. 4.1. Furthermore, ERA5 assimilates a partly different set of observations than the global data assimilation system in the ICON model (e.g. more satellite radiances) and does not use the Aeolus observations. It is well known that NWP models in the stratosphere are typically subject to large uncertainties. ERA5 was found to have a cold bias in the lower stratosphere and a warm bias near the stratopause (Hersbach et al., 2020). However, the increased number of assimilated GPSRO

155 bending angles in ERA5 since 2006 has significantly reduced this model bias, increasing confidence in using the stratospheric reanalyses for verification (Laloyaux et al., 2020).

The methods applied in this study are described according to Martin et al. (2022). The forecast error of an assimilation experiment X is calculated as:

$$e_i^X = forecast_i^X - reanalysis_i^{ERA5}, \quad (2)$$

160 with, X being either the CTRL or the EXP_A run and i representing the time step when the forecast and analysis are valid, respectively. The root-mean-squared error (RMSE) of the experiment X determines how strongly the forecast deviates from the verification data:

$$RMSE(e^X) = \sqrt{\overline{(e_i^X)^2}}, \quad (3)$$

where the overline is the mean over the requested dimension/dimensions - time, pressure level, latitude or longitude. Improvement or degradation of the forecast quality through the assimilation of Aeolus observations can then be assessed by the differences between $RMSE(e^{EXP_A})$ and $RMSE(e^{CTRL})$. Because the RMSE depends on the magnitude of forecasts and observations, the results are additionally verified by calculating the normalized RMSE differences:

$$e_{diff} = \frac{RMSE(e^{EXP_A}) - RMSE(e^{CTRL})}{RMSE(e^{CTRL})}. \quad (4)$$

3 Global forecast error reduction

170 The selection of particular regions of pronounced forecast error reduction due to the Aeolus observations, which are examined in the subsequent Section 4, is motivated by Figure 1 (according to Martin et al. (2022)).

Results of the OSE impact statistics evaluated by Martin et al. (2022) show the largest reduction in the zonal wind RMSE in the upper troposphere and lower stratosphere. Within the tropical band, the forecast errors of forecast lead times from 24 to 120 h are reduced by 2% up to almost 5% on average (Table 1). The spatial distribution of the relative RMSE reduction (Fig. 1a) reveals that above the tropical tropopause, the beneficial impact is primarily located around the equatorial band. On large scales, this area is affected by the quasi-biennial oscillation of the zonal wind, the QBO. Typically, the equatorial zonal wind between 70 and 10 hPa alternates between easterlies and westerlies, with the particular phase of the oscillation propagating downward over a period of 22 to 34 months. During the OSE period in summer 2020, the QBO cycling evolved as westerly jet between 50 and 30 hPa, found to be largely strengthened by the Aeolus observation (Martin et al., 2022). In Section 4.1, we 180 evaluate the hypothesis that there is a relation between the QBO phase change and the large impact of Aeolus.

Furthermore, large forecast error reduction can be found in the 300-hPa zonal wind in the midlatitudes in the Southern Hemisphere and the tropics with an average improvement of 1.7 -2.6%. The midlatitudes in the Southern Hemisphere overall show a fluctuating impact pattern. However, the most pronounced forecast error reduction appears around the storm track region downstream of South America. In the tropics, striking forecast error reduction is located around the Eastern Pacific 185 Ocean and the subtropical jet over South America at 300 hPa. The large-scale dynamics there are mainly dominated by the

coupled circulation system ENSO which is characterized by the interaction between surface temperatures and upper-level winds. Large systematic changes in the analysis over the Eastern Pacific due to the assimilation of Aeolus observations in the OSE were found by Martin et al. (2022) in the form of a strengthening of easterly winds. The OSE covers the onset of a shift in ENSO conditions which is generally associated with modifications in the zonal Walker circulation. This change in the wind pattern is expected to be the dynamical source of the large Aeolus impact and is discussed in more detail in the following (Sec. 4.2).

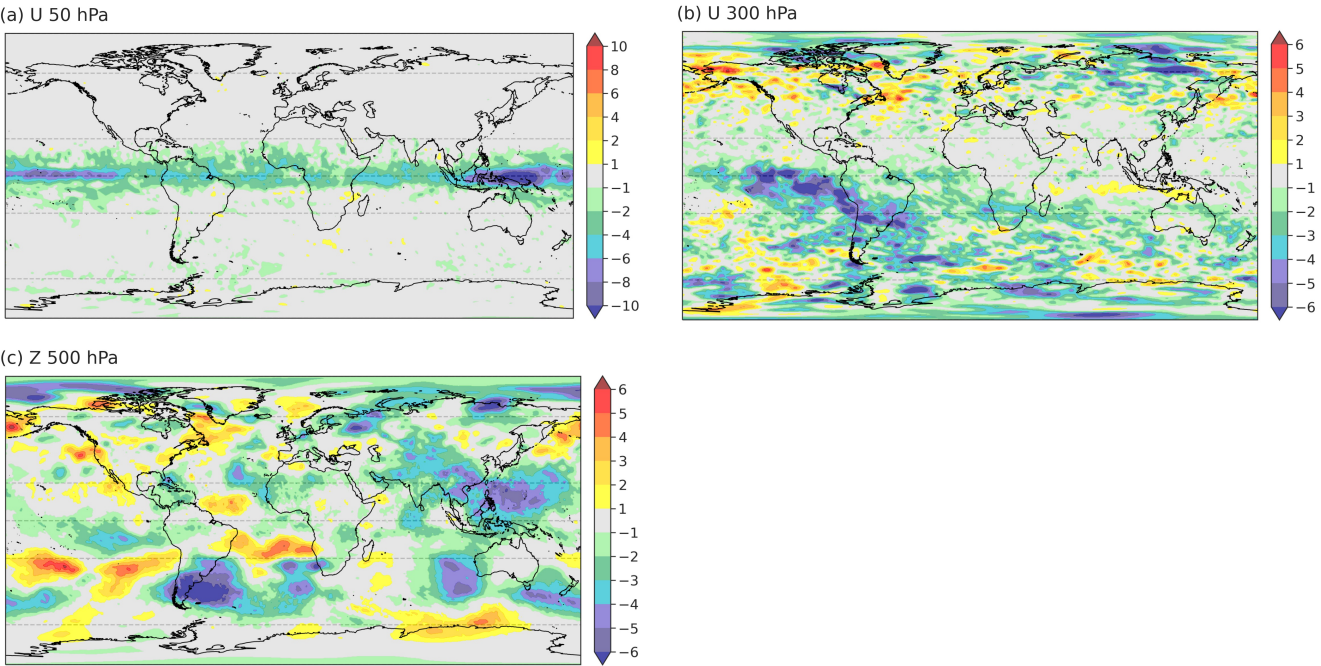


Figure 1. The mean relative differences in 24 - 120 h forecast RMSE between the EXP_A and the CTRL run [%] for 01 July 2020 to 30 September 2020, (a) 50-hPa zonal wind component (U), (b) 300-hPa zonal wind component (U), and (c) 500-hPa geopotential (Z).

	[-90°, -65°)	[-65°, -23.5°)	[-23.5°, 23.5°]	(23.5°, 65°]	(65°, 90°]
U 50 hPa	-0.78	-1.05	-4.84	-0.26	-0.54
U 300 hPa	-1.16	-1.72	-2.64	-0.47	-1.43
Z 500 hPa	-0.10	-1.71	-1.87	-0.74	-1.56

Table 1. Mean relative difference in 24 -120 h forecast RMSE between the EXP_A and the CTRL run [%] averaged over the polar, midlatitude and tropical region in the Northern and Southern Hemisphere for 50-hPa zonal wind component (U), 300-hPa zonal wind component (U), and 500-hPa geopotential (Z).

Further north, in the 500-hPa geopotential, large forecast error reduction occurs near the Tropic of Cancer ($\sim 23^\circ\text{N}$) in the western Pacific and Atlantic. These are regions of tropical cyclone activity in the experimental period. Furthermore, large improvement can be seen in the Southern Hemisphere storm track areas, such as the Indian Ocean, the eastern side of Australia and the region near 30°S over South America. On average, forecast errors are reduced by 1.9% in the tropics and by 1.7% (0.7%) in the Southern Hemisphere (Northern Hemisphere) midlatitudes. Overall, the mean impact pattern in the Northern Hemisphere is characterized by large variability likely related to fluctuations of the polar jet and the associated midlatitude circulation that partially obscures the mean error reduction. Large forecast error reduction over continents occurs over the Himalayan region, India and Eastern Asia. Moreover, both the zonal wind on 300 hPa and geopotential on 500 hPa show large improvements of 1.4 - 1.6% in the polar region in the Northern Hemisphere. Aeolus's impact in these regions may be investigated further in future investigations. In this study, we further examine the spatiotemporal evolution of forecast error reduction in midlatitudes to better understand the impact of Aeolus in relation to the general midlatitude circulation and to identify associated specific extratropical weather systems with a particular focus on the ET of tropical cyclones (Sec. 4.3).

4 Dynamical scenarios leading to pronounced forecast improvements

4.1 Impact on tropical stratospheric wind variations (QBO)

Systematic changes in the analysis field (Martin et al., 2022) and improvements in forecast quality of the stratospheric zonal wind field (Fig. 1) indicate an impact of the Aeolus observations on the QBO phase change from easterly to westerly that took place in summer 2020. In order to better monitor the QBO in 2020, the vertical range bin setting of Aeolus was adjusted to also allow for measurements up to 25 km in the tropics. This advanced setting was active in the tropical belt $\pm 10^\circ$ once a week for 24h only, from Wednesday, 01:00 am UTC until Thursday, 01:15 am UTC. After an unusual disruption of QBO cycling in winter 2019/2020 (Anstey et al., 2021), the regular oscillation in that stratospheric layer emerged again as an eastward jet around 20 August. Figure 2 focuses on the impact of Aeolus HLOS observation between 30 and 50 hPa around the equator, showing the time evolution. The Aeolus observations affect the change in zonal mean wind from easterly to westerly in the way that the evolved westerly winds are strengthened. The forecast errors of the CTRL run are fairly constant in time, only slightly varying between 4 and 6 m s^{-1} . On the other hand, the forecast errors of the EXP_A noticeably decrease with time. The relative differences in RMSE between EXP_A and CTRL already show improvements in the quality of the zonal wind forecast between 30 and 50 hPa by the Aeolus observations at the beginning of the OSE period. The reversal of the zonal wind direction is then accompanied by a marked reduction in the RMSE for all lead times. Towards the end of September, improvements of 10% to over 15% occur.

It should be taken into account that both the ERA5 reanalysis used for verification and the global model ICON exhibit large uncertainties in the tropical stratosphere, probably contributing to the pronounced impact of Aeolus observations. The QBO is mainly driven by a combination of upward-propagating low-frequency equatorial waves and inertia-gravity waves from the troposphere that dissipate and deposit momentum to the upper level zonal-mean zonal winds (Shepherd et al., 2018). However, a realistic representation of the wave, mean-flow interaction behind the QBO is typically limited by insufficient

225 vertical model resolution, uncertainties in parameterized processes such as tropical convection, and the sparseness of direct wind measurements in the tropics. Given the lack of direct wind observations in the area, the models there could be prone to biases.

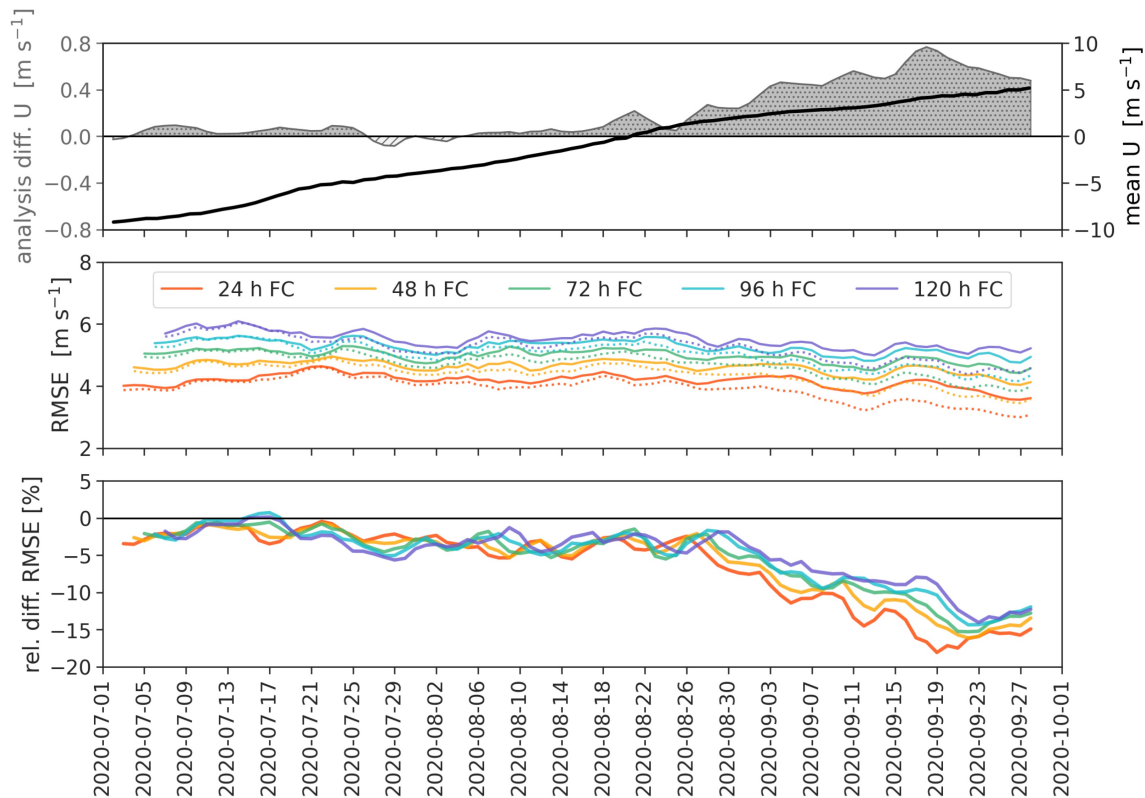


Figure 2. Time series for the tropical belt $\pm 10^\circ$ latitude between 30 and 50 hPa. Top row: the mean zonal wind (black line) and the mean analysis differences in the zonal wind between EXP_A and CTRL (shaded grey). Middle row: the RMSE for forecast lead times from 24 to 120 h for the CTRL (solid line) and the EXP_A (dotted line) run. Bottom row: relative differences in RMSE between EXP_A and CTRL for forecast lead times from 24 to 120 h.

Due to QBO teleconnections with other parts of the atmospheric system such as the polar vortex (Anstey and Shepherd, 2014; Baldwin et al., 2001; Gray et al., 2018) or tropical oscillations as, e.g., Madden-Julian Oscillation (MJO) (Martin et al., 2021b) and ENSO (Anstey et al., 2021), accurate prediction of the QBO by an additional observing system might also provide a meaningful source of longer-term predictive skill outside the tropics. Furthermore, several statistical studies showed that besides or in interaction with the ENSO, the QBO could also modulate the tropical cyclone activities over various oceans (Baldwin et al., 2001; Gray, 1984; Gray et al., 1992; Jury et al., 1999) and that the QBO west phase is usually associated with enhanced deep convection, both sides of the equator.

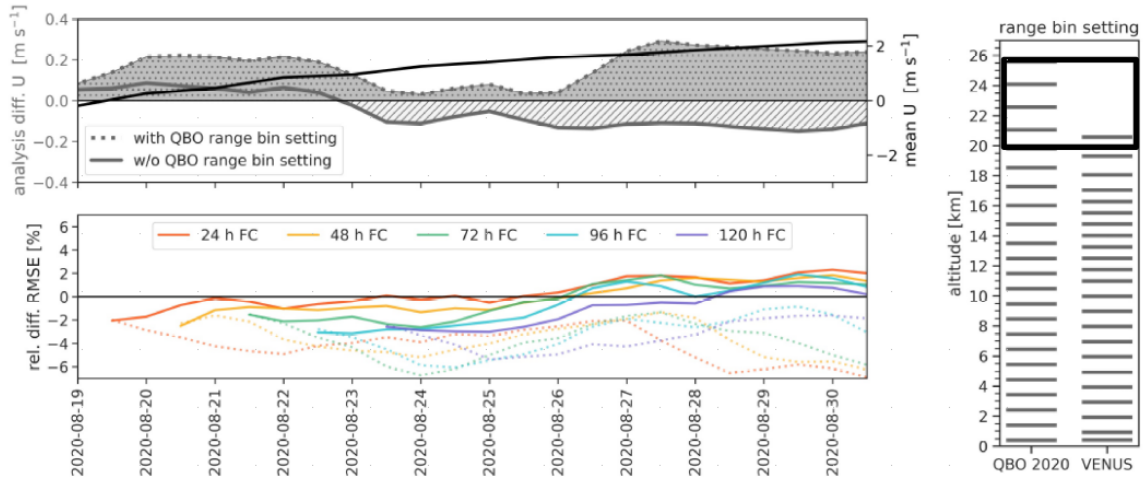


Figure 3. Time series for the tropical belt $\pm 10^\circ$ latitude between 30 and 50 hPa. Top row: the mean zonal wind (black line) and the mean analysis differences in the zonal wind between EXP_A and CTRL (shaded grey), with (dotted line) and without (solid line) the QBO range bin setting. Bottom row: relative differences in RMSE between EXP_A and CTRL for forecast lead times from 24 to 120 h, with (dotted line) and without (solid line) the QBO range bin setting. The distribution of the general tropical range bins (VENUS) and the advanced QBO setting is illustrated on the right, with the black rectangle highlighting the 30-50 hPa level.

Both accurate Aeolus wind measurements in the stratosphere and a good capture of upward propagating waves from the lower levels can cause the strong positive impact on the QBO phase change. To exclude the influence of the extended special QBO range bin setting, which amplifies the effect of the stratospheric Aeolus observations, another experimental run, with a shorter period of 14 days, was performed. For this, the Aeolus observations between Wednesday, 01:00 am UTC until Thursday, 01:15 am UTC were not used in the assimilation. Figure 3 displays the relevant time series from 18 August 2020 to 31 August 2020 of the analysis differences and the relative differences in RMSE for the tropical belt $\pm 10^\circ$ latitude between 30 and 50 hPa. The experiment with and without the QBO range bin setting are compared. On the right, in Figure 3 the distribution of the general tropical range bins (VENUS) and the advanced QBO setting is illustrated. The experiment's start covers the time when the QBO west phase manifested again. Whereas the Aeolus experiment with the QBO range bin setting shows a large influence in the analysis in the form of an intensification of the west winds, the exclusion of the high-resolution stratospheric Aeolus observations leads to a weakening of the west jet after a few days. Striking differences also appear in terms of forecast error for lead times from 24 to 120 h. Initially, both experiments show beneficial effects in the equatorial stratosphere, but with time the forecast error reduction of the experiment without QBO range bin setting decreases up to degradation of 2%. As the stratosphere is characterized by large model uncertainties, a longer OSE would be useful to draw robust conclusions. However, it is noteworthy that even within 14 days, the elimination of observations during two days of higher resolution Aeolus observations can have significant effects. This underscores the importance of the range bins settings for the Aeolus mission.

4.2 Impact on change in the ENSO state in the Eastern Pacific

In the the equatorial region, the ENSO is another important tropical oscillation pattern, whose interannual tropospheric variability influences both weather and climate on a global scale. It is characterized by irregular periodic fluctuations through a neutral phase between warm (El Niño) and cold (La Niña) extremes in sea surface temperature (SST) across the equatorial Pacific Ocean. In summer 2020, the state of ENSO changed from neutral to the La Niña state. The ENSO phases relate to the zonal Walker circulation, that is strengthened during La Niña events as the eastern Pacific is colder and the western Pacific is warmer than on average, leading to an enhanced rise of warm moist air over Indonesia and South America and an enhanced downward branch over the mid-Pacific. Figure 4 displays the time evolution of relative differences in 48 h forecast RMSE of the zonal wind component averaged over the equatorial Eastern Pacific [5°S - 5°N, 90°W - 160°W] as a function of altitude. The shift in the ENSO conditions is associated with a major change in the wind patterns of the tropical belt that appear to be strongly influenced by the assimilation of Aeolus wind observations. The 3-month average equatorial Pacific SST anomaly (Oceanic Niño Index (ONI)) is a common measure and NOAA's primary indicator for monitoring the state of ENSO. Around 8 August 2020, the SST anomaly, determined as the difference from the average ERA5 reanalysis from 1985 to 2015, exceeds the -0.5 K threshold, indicating the presence of La Niña conditions. This point in time is the beginning of a large forecast error reduction for upper-level zonal wind. The reduction in forecast error increases over the 14 days after the La Niña onset and extends into the middle troposphere. Enhanced improvements continue to occur afterwards and are also apparent in a shorter period before the onset. The largest error reduction in the 48 h forecast occurs about 48 h after the strongest negative increase in the SST anomaly, which corresponds to the time of initialization.

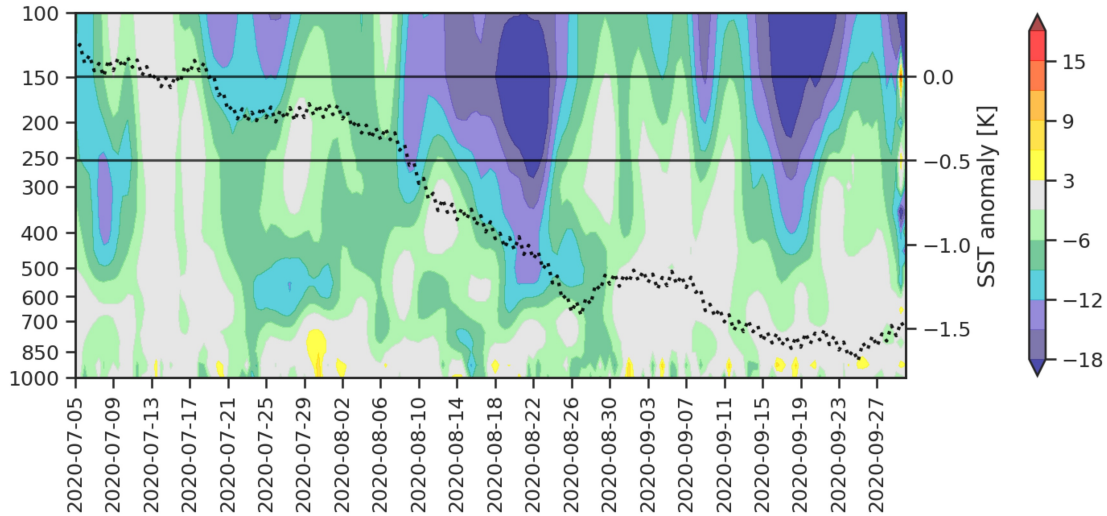


Figure 4. Relative differences in 48 h forecast RMSE of the zonal wind component [%] between EXP_A and CTRL [5°S - 5°N, 90°W - 160°W] as function of forecast time and pressure [hPa]. The black dotted line is the sea surface temperature (SST) anomaly from ERA5 reanalysis 1985 to 2015.

Together with the results of Section 4.1, this suggests that Aeolus particularly reduces uncertainty in the model representation in the beginning of variations in the large-scale circulation systems. The better representation of the ENSO pattern as provided by the HLOS winds in the ICON model is expected to have a variety of further beneficial impacts. The fluctuations in the ENSO pattern can, for example, greatly affect the location of tropical rainfall and wind patterns. Moreover, influences on the extratropics are possible via the interaction with Rossby wave trains (Hoskins and Karoly, 1981), the North Atlantic Oscillation (NAO) phase (Rogers, 1984) or the Pacific-North American Pattern (PNA) (Horel and Wallace, 1981), but also through planetary wave activity into the stratosphere (Iza et al., 2016).

275 4.3 Dynamical impact in the midlatitudes

Hovmöller diagrams are a common way of data plotting in meteorology to display both the change over time and the spatial variability of a variable. In particular, they serve to highlight the behaviour of atmospheric waves. To identify dynamical sources of the extratropical influence of Aeolus in the Northern Hemisphere, Figure 5 represents the latitudinal average between 25° and 60°N of the 250-hPa meridional wind field and the convective precipitation as a function of longitude and time from 08 July 2020 to 19 July 2020. The dashed black contour lines display the largest error reductions in the 48 h forecast of 500-hPa geopotential. At the beginning of the time period shown here, the tropical cyclone Fay, which originally formed from a surface low over the northern Gulf of Mexico, emerged into the western Atlantic Ocean. The storm intensified while moving northward, reaching its peak intensity on 10 July. Later that day, Fay made landfall over New Jersey and interacted with the midlatitude upper-level flow. The Hovmöller diagram shows pairs of green/blue and orange/red patches that form a clear banded pattern from 70° - 80°W around 10 July all the way to Europe on 15 July, representing individual troughs and ridges of an RWP. The contour lines related to the reduction in the 48 h forecast error of the 500-hPa geopotential are associated with this wave structure.

ET typically involves a complex interaction with the midlatitude baroclinic environment, which causes considerable changes in the characteristics of the cyclone (Grams et al., 2013). Interactions with the midlatitude waveguide can lead to increased forecast uncertainty, mainly associated with upper-level divergence, vertical wind shear and cirrus clouds (Jones et al., 2003). We, therefore, expect potential for beneficial impact from good Mie wind coverage with a comparably high resolution. In general, there is no commonly accepted definition of ET, but various classification factors have been proposed for a typical ET event. In Jones et al. (2003), a definition of a two-stage classification of ET based on Klein et al. (2000) can be found. Typically, when the cyclone is affected by vertical wind shear associated with the baroclinic zone, the axisymmetric structure of the tropical cyclone around the core is distorted, resulting in an asymmetry in the wind and thermal structures and consequently in the moisture, cloud, and precipitation fields. The upper-tropospheric divergent outflow, which appears as a cirrus cloud shield, may directly impact the large-scale midlatitude flow by interacting with the upstream trough of the midlatitude jet. Due to the tropical origin, low potential vorticity (PV) is advected by the divergent flow which leads to a strengthening of the meridional PV gradient. This results in an amplification of the jet streak and the development of a ridge-trough couplet downstream of the transitioning cyclone, which marks the generation of a new RWP or the modification of an existing one (Wirth et al., 2018). The

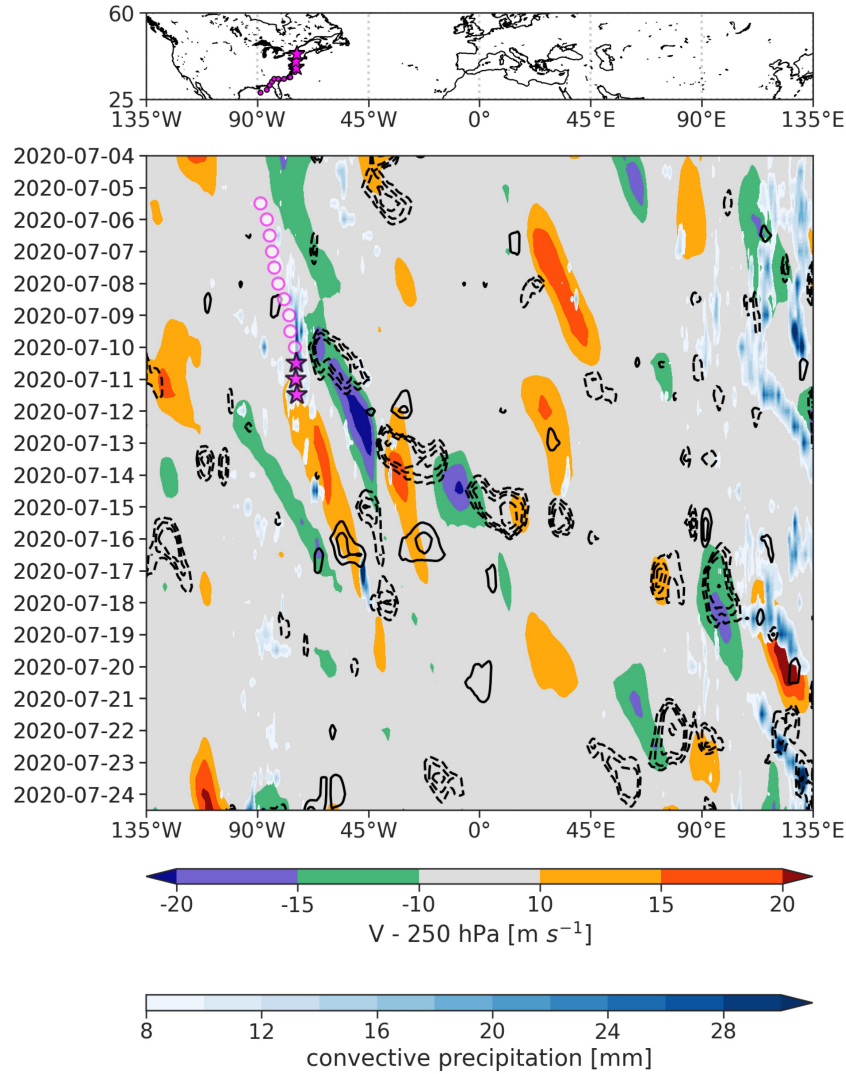


Figure 5. Hovmöller diagram of the 250-hPa meridional wind (color shading, in m s^{-1}) for 04 July 2020 to 24 July 2020 and the convective precipitation averaged between 25° and 60°N . The black contours are the largest differences of the 48 h forecast error of 500-hPa geopotential between EXP_A and CTRL (dashed: negative, solid: positive). The magenta circles mark the position of cyclone Fay, the stars highlight the onset of the ET and interaction with the midlatitude flow.

RWP then disperses further downstream and can contribute to the development of strong cyclogenesis or atmospheric blocking anticyclones (Riboldi et al., 2019). Therefore, ET associated with amplification of RWPs may also lead to high-impact weather in distant downstream regions (Keller et al., 2019). The many different atmospheric processes involved in ET events pose a major challenge for NWP models and can considerably reduce the skill of the medium-range forecasts downstream of the tropical cyclone (Jones et al., 2003).

305

It is suggested that the evolution of the reduction in the 48 h forecast error displayed in the Hovmöller diagram is related to the interaction of Fay undergoing ET with the midlatitude waveguide. The downward propagation of the forecast error reduction seems to be similar to the group velocity of the RWP. This picture fits the theory described by Keller et al. (2019), that uncertainties in the ability to predict ET events typically first manifest as uncertainties in the prediction of the strengthening of the downstream ridge and then propagate with the evolving RWP.

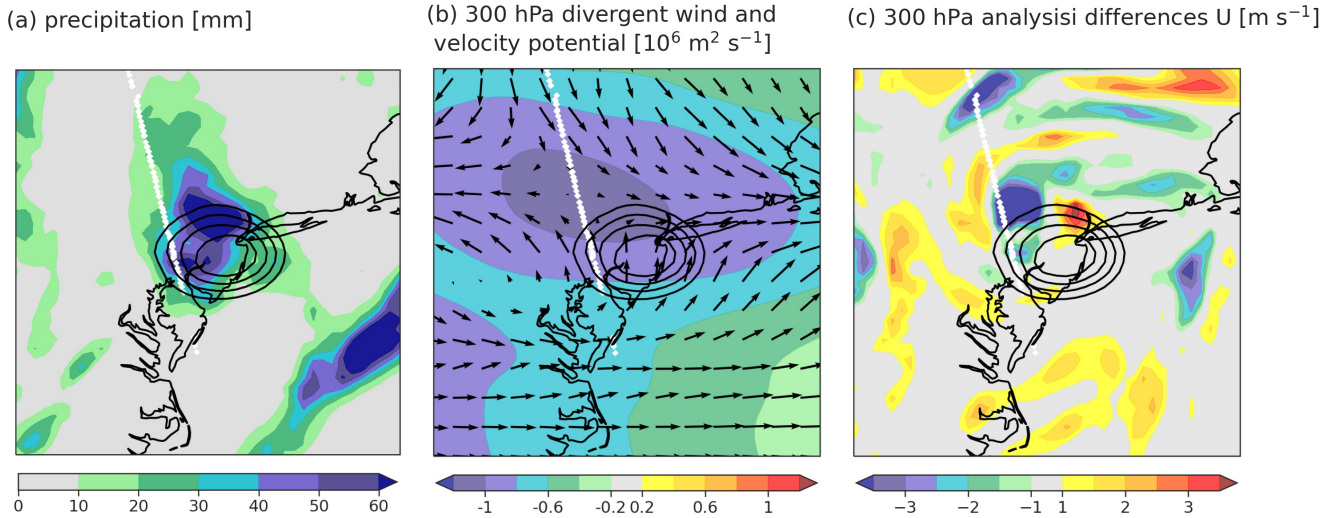


Figure 6. Precipitation (a), 300-hPa divergent wind (vectors) and velocity potential (b), and the analysis differences in 300-hPa zonal wind between EXP_A and CTRL (c) for 10 July 2020 12 UTC for the region around cyclone Fay [35° - 45° N, 80° - 70° W]. The black contours represent the minimum surface pressure.

310

Figure 6 focuses on the time around the onset of the ET of Fay. The contour lines are the minimum surface pressure showing Fay making landfall. Pronounced values in the divergent wind field of the upper troposphere (Fig. 6b) occur northwest of the cyclone center, representing the poleward expanding and anticyclonically rotating outflow. Characteristic for ET events are the regions of significant precipitation embedded in the cloud shield apparent in Figure 6a). The rain field tends to be located to the west of the cyclone center. The Mie wind observations from Aeolus assimilated at this time cover the area of the diverging flow very well, which could be the origin of the forecast improvements in the Hovmöller diagram right at the beginning of the RWP development. The differences in zonal wind on 300 hPa (Fig. 6c) exhibit an increased influence of Aeolus observations in terms of both west and east wind acceleration around the region of the interaction of the cyclone with the large-scale flow.

The forecast impact in course of the downstream development following the ET event is displayed in Figure 7 by the differences in forecast errors of the 500-hPa geopotential between EXP_A and CTRL for lead times from 24 to 144 h. All forecasts are initialized on 10 July 2020 12 UTC. Figure 7a shows the analysis differences at this time, when Hurricane Fay is located ahead of the upstream trough of the jet and the Aeolus track passes directly over the cyclone and trough front. Larger analysis influence is visible in the areas around the cyclone, especially at the trough axis. The evolution of the Aeolus impact

320

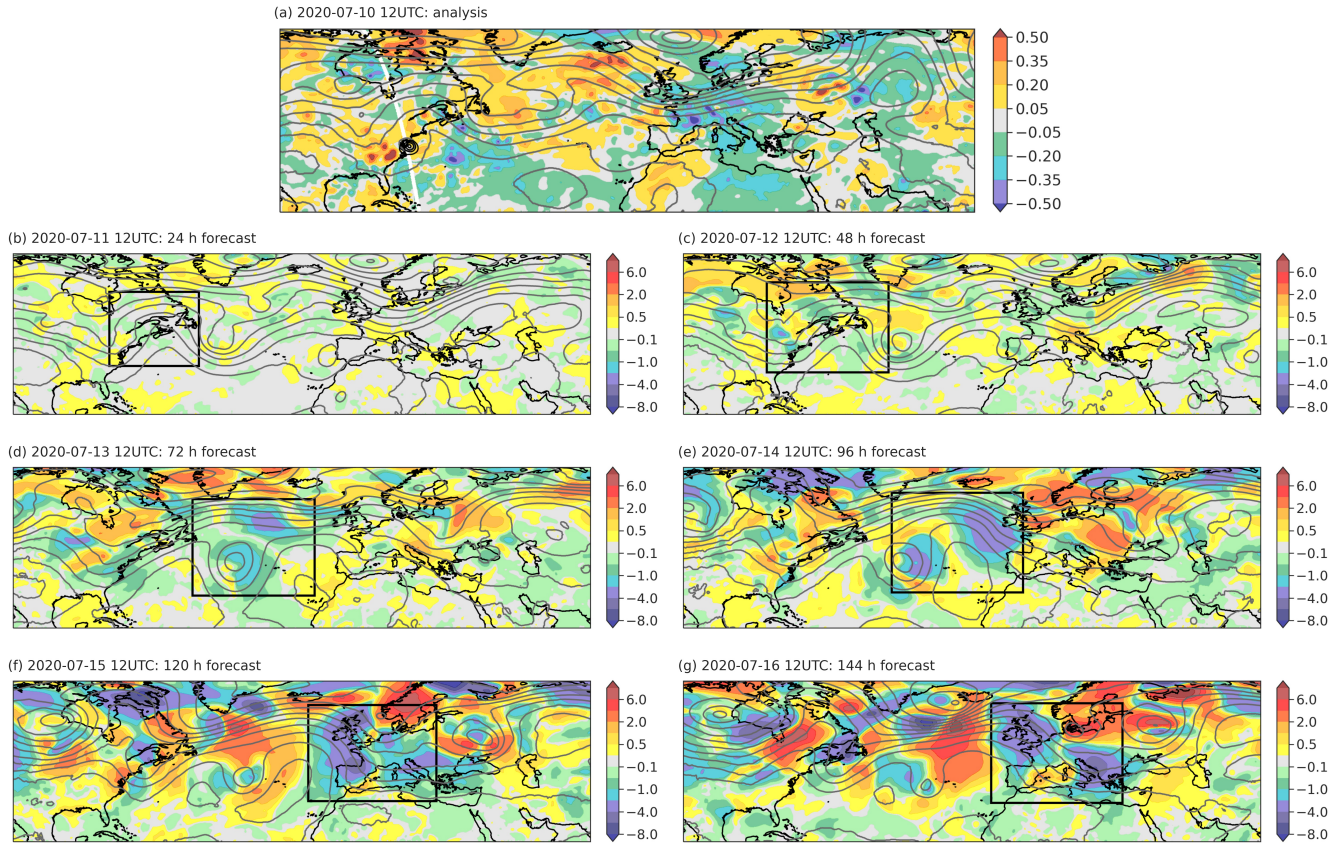


Figure 7. Downstream impact of Aeolus on 500-hPa geopotential from forecast start 10 July 2020 12 UTC for the region $[20^{\circ} - 70^{\circ}\text{N}, 110^{\circ}\text{W} - 70^{\circ}\text{E}]$. (a) The differences in analysis of between EXP_A and CTRL for 10 July 2020 12 UTC, the white line is the Aeolus track, the black contours are the minimum surface pressure, (b) differences in 24 h forecast error (EXP_A - CTRL) - 11 July 2020 12 UTC, (c) differences in 48 h forecast error - 12 July 2020 12 UTC, (d) differences in 72 h forecast error - 13 July 2020 12 UTC, (e) differences in 96 h forecast error - 14 July 2020 12 UTC, (f) differences in 120 h forecast error - 15 July 2020 12 UTC, (g) differences in 144 h forecast error - 16 July 2020 12 UTC. The box highlights the area of interest associated with the ET event; the grey contour lines represent the 500-hPa geopotential from ERA5 reanalysis in 5 gpm steps.

described in the following is believed to be related to either better coverage of upper troposphere outflow associated with the
 325 latent heat release of cyclone Fay or/and reduction of uncertainties in the dry baroclinic upper-level flow dynamics. In the 24
 h forecast (Fig. 7b), only small effects of the Aeolus observations on the midlatitude flow are visible in the region around the
 amplifying ridge, presumably related to the outflow. However, due to the assimilation cycling, the effects cannot be clearly
 assigned, but it is assumed that previous measurements and the cycling lead to differences in the cyclone as well as in the jet
 environment. The improvements become more distinct in the 48 h forecast (Fig. 7c) where the area of forecast error reduction
 330 moved towards the deepening trough downstream. One day later (Fig. 7d), a distinct RWP with a ridge–trough couplet and

cyclogenesis over the northern Atlantic Ocean developed. This cyclogenesis and the region of the jet streak above are associated with a large reduction of 72 h forecast error. Subsequently, the impact propagated downstream over the East Atlantic (Fig. 7e). Figure 7f shows a clear wave structure in the 500-hPa geopotential, from the east coast of America to Europa. The 120 and 144 h forecast error differences (Fig. 7f, 7g) highlight the area of increased error reduction spreading eastwards across the whole of Europe. This spatial perspective of the individual forecast times along the wave packet further supports the assumption that the downstream forecast improvement is related to the Aeolus observations in the area of the ET of Fay and preceding nearby observations.

The data denial experiment period includes a large part of the tropical cyclone season, and we detected additional ET cases associated with forecast error reduction by the assimilation of Aeolus observations. Figure 8 shows three further examples of Hovmöller diagrams for ET and the spatiotemporal evolution of RWP as well as differences in 500-hPa geopotential forecast error covering the time period of Hurricane Laura (Fig. 8a), Hurricane Paulette (Fig. 8b) and the two Typhoons Bavi and Maysak in the western Pacific (Fig. 8c). As in Figure 5, wave-like structures in the meridional wind component that form or intensify around the beginning of the ET are visible. However, the RWPs are not as pronounced as in Fay's ET event. Furthermore, the correspondence between the propagation velocity of the impact structures and the RWP does not seem to be as clear. But it was found that the area around the upper-level divergent outflow of the ET examples in Fig. 8a-c were all well-captured by the Aeolus Mie observations during the onset of the transition (not shown here). Therefore, some impact on the downstream development of the RWPs to Europe or for the Typhoons to America can be assumed. We also investigated the impact of Aeolus observations on tropical cyclone tracks. However, no significant improvements were found. This may be related to the lack of observations beneath clouds and consequently within and nearby the cyclone, but it could also be due to the need for large sample size when evaluating tropical cyclone tracks.

Furthermore, Figure 8d shows an example of an RWP developing in the region over southern South America, expected to be related to the clear structure of the largest forecast error reduction in 500-hPa geopotential. Typically, in the Southern Hemisphere winter season, cyclogenesis is associated with the subtropical jet in the lee of the Andes in South America (Hoskins and Hodges, 2005). Berbery and Barros (2002) discussed the strong moisture transport in winter and spring from the tropics into the La Plata River basin on the eastern side of the Andes and the importance of associated latent heat release for subtropical cyclogenesis process. The increased beneficial impact of the Aeolus observations in this region along the subtropical waveguide on the Southern Hemisphere has already been shown in the mean forecast error reduction in 500-hPa geopotential in Section 3 (Fig. 1). This might be related to good Mie wind observations in moist areas associated with cyclogenesis, capturing the onset or modification of orographically excited RWPs. Overall, there is significantly less knowledge available for the storm tracks in the Southern Hemisphere than in Northern Hemisphere, which has been observed and examined more comprehensively in the past.

The importance of upscale error growth from convective to larger atmospheric scales limiting the predictability in NWP is discussed in several recent studies (e.g. Hohenegger and Schär, 2007; Rodwell et al., 2013; Selz and Craig, 2015; Selz et al., 2022). Selz et al. (2022) found that latent heat release in convective systems and the divergent component of the atmospheric flow dominate the error growth with respect to physical processes. It is assumed that accurate observations of the divergent

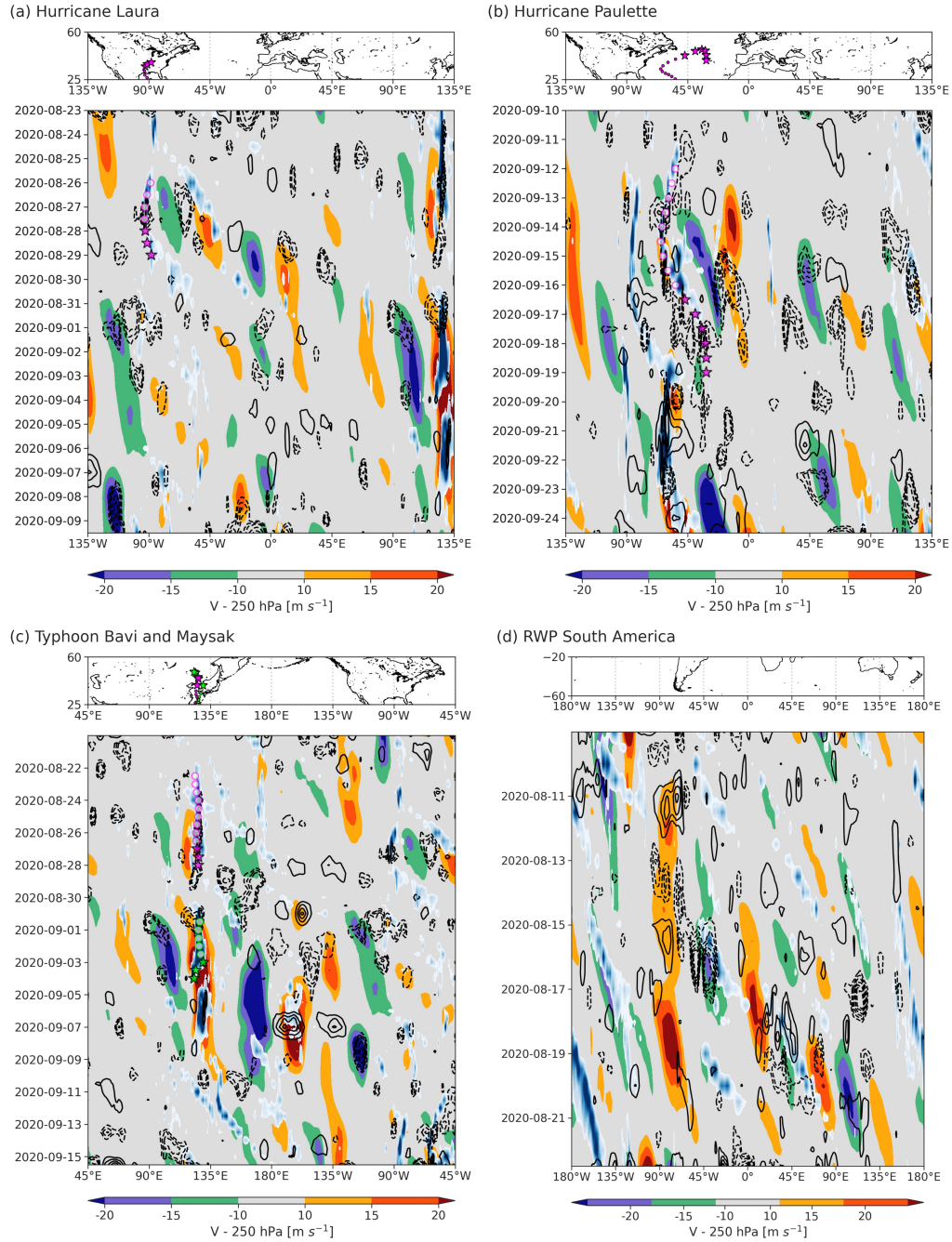


Figure 8. Same as Figure 5 for the ET event of (a) Hurricane Laura, (b) tropical cyclone Paulette, and (c) Typhoon Bavi and Maysak, and (d) an RWP development around the cyclogenesis region over South America.

wind field as expected from the Aeolus winds can reduce the uncertainty of the initial conditions around mesoscale convective ET events, but also in cyclogenesis regions in other parts of the world. Overall, the results of this section show potential for further investigation of the dynamical effects of the assimilation of the Aeolus wind observations for both the higher latitudes in the Northern and Southern Hemisphere.

370 **5 Conclusions**

The observations of the DWL satellite mission Aeolus provide wind profiles in the troposphere and the lower stratosphere with quasi-global coverage. A three-month OSE from July 2020 to October 2020 was conducted to evaluate the impact of the Aeolus horizontal line-of-sight (HLOS) wind observations in the ICON system's operational global data assimilation system. In a preceding study (Martin et al., 2022), it has been shown that the Aeolus observations improve both analyses and forecasts, 375 with the largest impact in the tropics around the tropopause level. However, a relatively large forecast error reduction of up to 2% was also found from global statistics in the midlatitudes. So far, the dynamical processes responsible for improving the forecast have only been given little consideration. Therefore, the main objective of this study is to highlight indications of atmospheric features and dynamical changes constituting pathways for significant impact of the Aeolus observations for future research studies. Based on the global statistical analysis, regions of enhanced forecast error reduction were chosen to discuss 380 the underlying dynamics.

Two important large-scale tropical circulation systems - QBO and ENSO - appear to be very well-measured by Aeolus during the time that is associated with a shift in the oscillatory phase. The change in the stratospheric jet from easterly to westerly in August 2020 was found to be related to the large positive impact of the Aeolus winds. Further investigation suggests that the impact of 10 - 15% in the equatorial band around 50 hPa is largely amplified by a special QBO range bin setting that has been 385 adjusted to account for atmospheric winds up to altitudes of 25 km one day per week. This would mean that the improvements are mainly due to good measurements of the upper atmosphere rather than improved detection of propagating waves from the troposphere. However, a longer accompanying experiment would be necessary for a precise assessment, especially since the stratosphere generally exhibits large uncertainties in NWP models. Furthermore, in August 2020, the tropical troposphere in the Pacific Ocean was characterized by a large-scale dynamic variability. The Southern Oscillation state changed from the 390 normal to the La Niña phase. The associated strengthening of upper and mid-tropospheric wind patterns in the region of the Eastern Pacific related to the zonal Walker circulation is advantageously captured by Aeolus. QBO and ENSO are typically characterized by teleconnections with other atmospheric systems through, e.g. other oscillation phenomena in the extratropics or wave activity. Therefore, the variability in the tropics can lead to large uncertainties in many parts of the world. In addition to short- and medium-range NWP, seasonal and sub-seasonal forecasts can benefit from the potential of the Aeolus observations 395 to better represent the initial state of fluctuations in such large-scale circulation systems.

In addition to the tropics, the influence of Aeolus observations on midlatitude dynamics was investigated. Although especially continents are already comparably well observed by other observation types, the HLOS winds have, on average, a relatively large beneficial impact. However, the spatial distribution shows that the effects appear to be partially masked by

fluctuations in the three-month mean flow. Systematically positive impact particularly stands out in storm track regions in the
400 Southern Hemisphere, but some average improvements are also seen in the Northern Hemisphere. Furthermore, it was found
that the development of a RWP likely associated with cyclogenesis in the lee of the Andes in South America may be related to
the reduction of large forecast errors.

For future studies, we recommend long-term experiments in combination with feature-based diagnostics to further investi-
gate the influence of HLOS winds on tropical cyclones and the upscale interaction and representation of error growth. Since
405 tropical cyclones are not common events, a long integration period is necessary to achieve a sufficiently large sample and thus
robust results. A longer OSE would also be required to further study the impact on other large-scale convective circulation
systems, such as the Madden-Julian-Oscillation (MJO), that affect weekly to monthly forecast skills. Besides the Northern
Hemisphere and tropical dynamics, a better assessment of the large impacts found in the southern parts of the world would
be an interesting research study, especially since the causes of forecast busts in the Northern Hemisphere are much better
410 understood.

Data availability. Aeolus data can be obtained from the ESA Aeolus web portal, <https://aeolus.services/>. ERA5 data can be obtained from
the Copernicus Climate Data Store, <https://cds.climate.copernicus.eu/>. The OSE dataset (created by Alexander Cress) can be made available
upon reasonable request.

Author contributions. A.M. performed the data analysis and prepared the main part of the publication. M.W. supervised the work, conceived
415 the research concept and contributed to the development of methods and analysis of the data. A.C. conducted the experiment at DWD and
provided important information on their use and interpretation. All co-authors engaged in discussions and contributed to the interpretation of
the results.

Competing interests. The authors affirm that they have no conflict of interest.

Acknowledgements. This work was funded by the German Federal Ministry for Economic Affairs and Energy (BMWi) under grant number
420 (FKZ) 50EE1721A and further supported by the Transregional Collaborative Research Center Waves to Weather (W2W) (SFB/TRR165)
funded by the German Research Foundation (DFG). We want to thank the European Space Agency (ESA) for providing the datasets and
the experts from the Experimental Validation And Assimilation (EVAA) consortium (LMU, DWD, DLR), the Data Innovation and Science
Cluster (DISC), and the Aeolus Cal/Val community for valuable discussions, particularly: Oliver Reitebuch, Michael Rennie and Alexander
Geiss. Furthermore, the exchange of tools and discussion with Maurus Borne and Peter Knippertz from W2W is greatly appreciated.

- Anstey, J. A. and Shepherd, T. G.: High-latitude influence of the quasi-biennial oscillation, *Quarterly Journal of the Royal Meteorological Society*, 140, 1–21, <https://doi.org/10.1002/qj.2132>, 2014.
- Anstey, J. A., Banyard, T. P., Butchart, N., Coy, L., Newman, P. A., Osprey, S., and Wright, C. J.: Prospect of Increased Disruption to the QBO in a Changing Climate, *Geophysical Research Letters*, 48, e2021GL093058, <https://doi.org/10.1029/2021GL093058>, 2021.
- 430 Baker, W. E., Atlas, R., Cardinali, C., Clement, A., Emmitt, G. D., Gentry, B. M., Hardesty, R. M., Källén, E., Kavaya, M. J., Langland, R., Ma, Z., Masutani, M., McCarty, W., Pierce, R. B., Pu, Z., Riishojgaard, L. P., Ryan, J., Tucker, S., Weissmann, M., and Yoe, J.: Lidar-measured wind profiles: The missing link in the Global Observing System, *Bulletin of the American Meteorological Society*, 95, 543–564, <https://doi.org/10.1175/BAMS-D-12-00164.1>, 2014.
- Baldwin, M. P., Gray, L. J., Dunkerton, T. J., Hamilton, K., Haynes, P. H., Randel, W. J., Holton, J. R., Alexander, M. J., Hirota, I., Horinouchi, T., Jones, D. B. A., Kinnarsley, J. S., Marquardt, C., Sato, K., and Takahashi, M.: The quasi-biennial oscillation, *Reviews of Geophysics*, 39, 179–229, <https://doi.org/10.1029/1999RG000073>, 2001.
- 435 Bauer, P., Thorpe, A., and Brunet, G.: The quiet revolution of numerical weather prediction, *Nature*, 525, 47–55, <https://doi.org/10.1038/nature14956>, 2015.
- Berbery, E. H. and Barros, V. R.: The Hydrologic Cycle of the La Plata Basin in South America, *Journal of Hydrometeorology*, 3, 630 – 645, [https://doi.org/10.1175/1525-7541\(2002\)003<0630:THCOTL>2.0.CO;2](https://doi.org/10.1175/1525-7541(2002)003<0630:THCOTL>2.0.CO;2), 2002.
- 440 Desroziers, G., Berre, L., Chapnik, B., and Poli, P.: Diagnosis of observation, background and analysis-error statistics in observation space, *Quarterly Journal of the Royal Meteorological Society*, 131, 3385–3396, <https://doi.org/10.1256/qj.05.108>, 2005.
- ESA: Atmospheric dynamics mission. Mission Selection Rep., ESA SP-1233(4), 1999.
- ESA: ADM-Aeolus Science Report, ESA SP-1311, 121 p., <https://earth.esa.int/documents/10174/1590943/AEOL002.pdf>, 2008.
- 445 ESA: ADM-Aeolus Mission Requirements Documents, ESA EOP-SM/2047, 57 p., http://esamultimedia.esa.int/docs/EarthObservation/ADM-Aeolus_MRD.pdf, 2016.
- Garrett, K., Liu, H., Ide, K., Hoffman, R. N., and Lukens, K. E.: Optimization and impact assessment of Aeolus HLOS wind assimilation in NOAA’s global forecast system, *Quarterly Journal of the Royal Meteorological Society*, 148, 2703–2716, <https://doi.org/10.1002/qj.4331>, 2022.
- 450 Grams, C. M., Jones, S. C., Davis, C. A., Harr, P. A., and Weissmann, M.: The impact of Typhoon Jangmi (2008) on the midlatitude flow. Part I: Upper-level ridgebuilding and modification of the jet, *Quarterly Journal of the Royal Meteorological Society*, 139, 2148–2164, <https://doi.org/10.1002/qj.2091>, 2013.
- Gray, L. J., Anstey, J. A., Kawatani, Y., Lu, H., Osprey, S., and Schenzinger, V.: Surface impacts of the Quasi Biennial Oscillation, *Atmospheric Chemistry and Physics*, 18, 8227–8247, <https://doi.org/10.5194/acp-18-8227-2018>, 2018.
- 455 Gray, W. M.: Atlantic Seasonal Hurricane Frequency. Part I: El Niño and 30 mb Quasi-Biennial Oscillation Influences, *Monthly Weather Review*, 112, 1649 – 1668, [https://doi.org/10.1175/1520-0493\(1984\)112<1649:ASHFPI>2.0.CO;2](https://doi.org/10.1175/1520-0493(1984)112<1649:ASHFPI>2.0.CO;2), 1984.
- Gray, W. M., Sheaffer, J. D., and Knaff, J. A.: Influence of the Stratospheric QBO on ENSO Variability, *Journal of the Meteorological Society of Japan. Ser. II*, 70, 975–995, https://doi.org/10.2151/jmsj1965.70.5_975, 1992.
- Hersbach, H., Bell, B., Berrisford, P., Hirahara, S., Horányi, A., Muñoz-Sabater, J., Nicolas, J., Peubey, C., Radu, R., Schepers, D., Simmons, A., Soci, C., Abdalla, S., Abellan, X., Balsamo, G., Bechtold, P., Biavati, G., Bidlot, J., Bonavita, M., De Chiara, G., Dahlgren, P., Dee, D., Diamantakis, M., Dragani, R., Flemming, J., Forbes, R., Fuentes, M., Geer, A., Haimberger, L., Healy, S., Hogan, R. J.,
- 460

- Hólm, E., Janisková, M., Keeley, S., Laloyaux, P., Lopez, P., Lupu, C., Radnoti, G., de Rosnay, P., Rozum, I., Vamborg, F., Villaume, S., and Thépaut, J.-N.: The ERA5 global reanalysis, *Quarterly Journal of the Royal Meteorological Society*, 146, 1999–2049, <https://doi.org/10.1002/qj.3803>, 2020.
- 465 Hohenegger, C. and Schär, C.: Predictability and Error Growth Dynamics in Cloud-Resolving Models, *Journal of the Atmospheric Sciences*, 64, 4467 – 4478, 10.1175/2007JAS2143.1, 2007.
- Horel, J. D. and Wallace, J. M.: Planetary-Scale Atmospheric Phenomena Associated with the Southern Oscillation, *Monthly Weather Review*, 109, 813 – 829, 10.1175/1520-0493(1981)109<0813:PSAPAW>2.0.CO;2, 1981.
- Hoskins, B. J. and Hodges, K. I.: A New Perspective on Southern Hemisphere Storm Tracks, *Journal of Climate*, 18, 4108 – 4129,
470 <https://doi.org/10.1175/JCLI3570.1>, 2005.
- Hoskins, B. J. and Karoly, D. J.: The Steady Linear Response of a Spherical Atmosphere to Thermal and Orographic Forcing, *Journal of Atmospheric Sciences*, 38, 1179 – 1196, 10.1175/1520-0469(1981)038<1179:TSLROA>2.0.CO;2, 1981.
- Iza, M., Calvo, N., and Manzini, E.: The Stratospheric Pathway of La Niña, *Journal of Climate*, 29, 8899 – 8914, 10.1175/JCLI-D-16-0230.1, 2016.
- 475 Jones, S. C., Harr, P. A., Abraham, J., Bosart, L. F., Bowyer, P. J., Evans, J. L., Hanley, D. E., Hanstrum, B. N., Hart, R. E., Lalaurette, F., Sinclair, M. R., Smith, R. K., and Thorncroft, C.: The Extratropical Transition of Tropical Cyclones: Forecast Challenges, Current Understanding, and Future Directions, *Weather and Forecasting*, 18, 1052 – 1092, [https://doi.org/10.1175/1520-0434\(2003\)018<1052:TETOTC>2.0.CO;2](https://doi.org/10.1175/1520-0434(2003)018<1052:TETOTC>2.0.CO;2), 2003.
- Jury, M. R., Pathack, B., and Parker, B.: Climatic Determinants and Statistical Prediction of Tropical Cyclone Days in the Southwest Indian
480 Ocean, *Journal of Climate*, 12, 1738–1746, <http://www.jstor.org/stable/26244387>, 1999.
- Keller, J. H., Grams, C. M., Riemer, M., Archambault, H. M., Bosart, L., Doyle, J. D., Evans, J. L., Galarneau, T. J., Griffin, K., Harr, P. A., Kitabatake, N., McTaggart-Cowan, R., Pantillon, F., Quinting, J. F., Reynolds, C. A., Ritchie, E. A., Torn, R. D., and Zhang, F.: The Extratropical Transition of Tropical Cyclones. Part II: Interaction with the Midlatitude Flow, Downstream Impacts, and Implications for Predictability, *Monthly Weather Review*, 147, 1077 – 1106, <https://doi.org/10.1175/MWR-D-17-0329.1>, 2019.
- 485 Klein, P. M., Harr, P. A., and Elsberry, R. L.: Extratropical Transition of Western North Pacific Tropical Cyclones: An Overview and Conceptual Model of the Transformation Stage, *Journal of Weather and Forecasting*, 15, 373 – 395, [https://doi.org/10.1175/1520-0434\(2000\)015<0373:ETOWNP>2.0.CO;2](https://doi.org/10.1175/1520-0434(2000)015<0373:ETOWNP>2.0.CO;2), 2000.
- Laloyaux, P., Bonavita, M., Dahoui, M., Farnan, J., Healy, S., Hólm, E., and Lang, S. T. K.: Towards an unbiased stratospheric analysis, *Quarterly Journal of the Royal Meteorological Society*, 146, 2392–2409, <https://doi.org/10.1002/qj.3798>, 2020.
- 490 Laroche, S. and St-James, J.: Impact of the Aeolus Level-2B horizontal line-of-sight winds in the Environment and Climate Change Canada global forecast system, *Quarterly Journal of the Royal Meteorological Society*, 148, 2047–2062, <https://doi.org/10.1002/qj.4300>, 2022.
- Marseille, G., Stoffelen, A., and Barkmeijer, J.: Impact assessment of prospective spaceborne Doppler wind lidar observation scenarios, *Tellus A: Dynamic Meteorology and Oceanography*, 60A, 234–248, <https://doi.org/10.1111/j.1600-0870.2007.00289.x>, 2008a.
- Marseille, G., Stoffelen, A., and Barkmeijer, J.: A cycled sensitivity observing system experiment on simulated Doppler wind lidar data during
495 the 1999 Christmas storm ‘Martin’, *Tellus A: Dynamic Meteorology and Oceanography*, 60A, 249–260, <https://doi.org/10.1111/j.1600-0870.2007.00290.x>, 2008b.
- Martin, A., Weissmann, M., Reitebuch, O., Rennie, M., Geiß, A., and Cress, A.: Validation of Aeolus winds using radiosonde observations and numerical weather prediction model equivalents, *Atmospheric Measurement Techniques*, 14, 2167–2183, <https://doi.org/10.5194/amt-14-2167-2021>, 2021a.

- 500 Martin, A., Weissmann, M., and Cress, A.: Impact of assimilating Aeolus observations in the global model ICON: A global statistical overview, <https://ucloud.univie.ac.at/index.php/s/DIP0XxSgKA6eXek>, 2022.
- Martin, Z., Son, S. W., Butler, A., Hendon, H., Kim, H., Sobel, A., Yoden, S., and Zhang, C.: The influence of the quasi-biennial oscillation on the Madden–Julian oscillation, *Nature Reviews Earth & Environment*, 2, 477–489, <https://doi.org/10.1038/s43017-021-00173-9>, 2021b.
- Pourret, V., Šavli, M., Mahfouf, J.-F., Raspaud, D., Doerenbecher, A., Bénichou, H., and Payan, C.: Operational assimilation of
505 Aeolus winds in the Météo-France global NWP model ARPEGE, *Quarterly Journal of the Royal Meteorological Society*, n/a, <https://doi.org/10.1002/qj.4329>, 2022.
- Pu, Z., Zhang, L., and Emmitt, G. D.: Impact of airborne Doppler wind lidar profiles on numerical simulations of a tropical cyclone, *Geophysical Research Letters*, 37, <https://doi.org/10.1029/2009GL041765>, 2010.
- Reinert, D., Prill, F., Frank, H., Denhard, M., Baldauf, M., Schraff, C., Gebhardt, C., Marsigli, C., and Zängl, G.: DWD Database Reference
510 for the Global and Regional ICON and ICON-EPS Forecasting System, https://www.dwd.de/DWD/forschung/nw/fepub/icon_database_main.pdf, 2023.
- Rennie, M., Isaksen, L., Weiler, F., de Kloe, J., Kanitz, T., and Reitebuch, R.: The impact of Aeolus wind retrievals on ECMWF global weather forecast, *Quarterly Journal of the Royal Meteorological Society*, pp. 1–32, <https://doi.org/10.1002/qj.4142>, 2021.
- Riboldi, J., Grams, C. M., Riemer, M., and Archambault, H. M.: A Phase Locking Perspective on Rossby Wave Amplification and At-
515 mospheric Blocking Downstream of Recurring Western North Pacific Tropical Cyclones, *Monthly Weather Review*, 147, 567 – 589, <https://doi.org/10.1175/MWR-D-18-0271.1>, 2019.
- Rodwell, M. J., Magnusson, L., Bauer, P., Bechtold, P., Bonavita, M., Cardinali, C., Diamantakis, M., Earnshaw, P., Garcia-Mendez, A., Isaksen, L., Källén, E., Klocke, D., Lopez, P., McNally, T., Persson, A., Prates, F., and Wedi, N.: Characteristics of Occasional Poor Medium-Range Weather Forecasts for Europe, *Bulletin of the American Meteorological Society*, 94, 1393 – 1405, <https://doi.org/10.1175/BAMS-D-12-00099.1>, 2013.
- 520 Rogers, J. C.: The Association between the North Atlantic Oscillation and the Southern Oscillation in the Northern Hemisphere, *Monthly Weather Review*, 112, 1999 – 2015, 10.1175/1520-0493(1984)112<1999:TABTNA>2.0.CO;2, 1984.
- Selz, T. and Craig, G. C.: Upscale Error Growth in a High-Resolution Simulation of a Summertime Weather Event over Europe, *Monthly Weather Review*, 143, 813 – 827, 10.1175/MWR-D-14-00140.1, 2015.
- 525 Selz, T., Riemer, M., and Craig, G.: The transition from practical to intrinsic predictability of midlatitude weather, *Journal of the Atmospheric Sciences*, 10.1175/JAS-D-21-0271.1, 2022.
- Shepherd, T., Polichtchouk, I., Hogan, R., and Simmons, A.: Report on Stratosphere Task Force, ECMWF Technical Memoranda, <https://doi.org/10.21957/0vkp0t1xx>, 2018.
- Stoffelen, A., Marseille, G.-J., Bouttier, F., Vasiljevic, D., de Haan, S., and Cardinali, C.: ADM-Aeolus Doppler wind lidar observing system
530 simulation experiment, *Quarterly Journal of the Royal Meteorological Society*, 132, 1927–1947, <https://doi.org/10.1256/qj.05.83>, 2006.
- Tan, D. G. H., Andersson, E., Fisher, M., and Isaksen, L.: Observing-system impact assessment using a data assimilationensemble technique: application to the ADM Aeolus wind profiling mission, *Quarterly Journal of the Royal Meteorological Society*, 133, 381–390, <https://doi.org/10.1002/qj.43>, 2007.
- Tan, D. G. H., Andersson, E., Kloe, J. D., Marseille, G.-J., Stoffelen, A., Poli, P., Denneulin, M.-L., Dabas, A., Huber, D., Reitebuch, O.,
535 Flamant, P., Rille, O. L., and Nett, H.: The ADM-Aeolus wind retrieval algorithms, *Tellus A: Dynamic Meteorology and Oceanography*, 60, 191–205, <https://doi.org/10.1111/j.1600-0870.2007.00285.x>, 2008.

- Šavli, M., Pourret, V., Payan, C., and Mahfouf, J.-F.: Sensitivity of Aeolus HLOS winds to temperature and pressure specification in the L2B processor, *Atmospheric Measurement Techniques*, 14, 4721–4736, <https://doi.org/10.5194/amt-14-4721-2021>, 2021.
- Žagar, N.: Assimilation of equatorial waves by line of sight wind observations, *Journal of Atmospheric Science*, 61, 1877–1893, [https://doi.org/10.1175/1520-0469\(2004\)061<1877:AOEWBL>2.0.CO;2](https://doi.org/10.1175/1520-0469(2004)061<1877:AOEWBL>2.0.CO;2), 2004.
- Žagar, N., Stoffelen, A., Marseille, G., Accadia, C., and Schlüssel, P.: Impact Assessment of Simulated Doppler Wind Lidars with a Multivariate Variational Assimilation in the Tropics, *Monthly Weather Review*, 136, 2443–2460, <https://doi.org/10.1175/2007MWR2335.1>, 2008.
- Weiler, F., Rennie, M., Kanitz, T., Isaksen, L., Checa, E., de Kloe, J., Okunde, N., and Reitebuch, O.: Correction of wind bias for the lidar on board Aeolus using telescope temperatures, *Atmospheric Measurement Techniques*, 14, 7167–7185, <https://doi.org/10.5194/amt-14-7167-2021>, 2021.
- Weissmann, M. and Cardinali, C.: Impact of airborne Doppler lidar observations on ECMWF forecasts, *Quarterly Journal of the Royal Meteorological Society*, 133, 107–116, <https://doi.org/10.1002/qj.16>, 2007.
- Weissmann, M., Langland, R. H., Cardinali, C., Pauley, P. M., and Rahm, S.: Influence of airborne Doppler wind lidar profiles near Typhoon Sinlaku on ECMWF and NOGAPS forecasts, *Quarterly Journal of the Royal Meteorological Society*, 138, 118–130, <https://doi.org/10.1002/qj.896>, 2012.
- Wirth, V., Riemer, M., Chang, E. K. M., and Martius, O.: Rossby Wave Packets on the Midlatitude Waveguide—A Review, *Monthly Weather Review*, 146, 1965 – 2001, <https://doi.org/10.1175/MWR-D-16-0483.1>, 2018.
- Zängl, G., Reinert, D., Rípodas, P., and Baldauf, M.: The ICON (ICOsahedral Non-hydrostatic) modelling framework of DWD and MPI-M: Description of the non-hydrostatic dynamical core, *Quarterly Journal of the Royal Meteorological Society*, 141, 563–579, <https://doi.org/10.1002/qj.2378>, 2015.